Monolayer support control demonstrates metal-support interactions in heterogeneous catalysts

Emmett D. Goodman[1]*, Arun S. Asundi[1]*, Adam S. Hoffman[2], Karen C. Bustillo[3], Jonathan F. Stebbins[4], Simon R. Bare[2], Stacey F. Bent[1], Matteo Cargnello[1]

[1]*Department of Chemical Engineering, Stanford University, Stanford, California 94305, United States*
[2]*SSRL, SLAC National Accelerator Laboratory, Menlo Park, California 94025, United States*
[3]*National Center for Electron Microscopy, Molecular Foundry, Lawrence Berkeley National Laboratory, Berkeley, California 94720, United States*
[4]*Department of Geological Sciences, Stanford University, Stanford, California 94305, United States*

*Authors contributed equally.
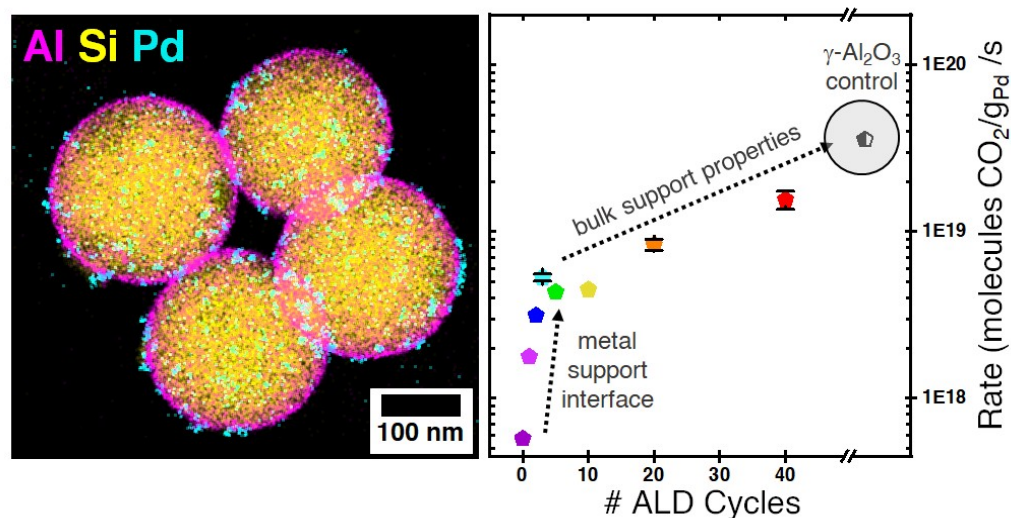
Abstract

Electronic and geometric interactions between active and support phases are critical in determining the activity of heterogeneous catalysts, but metal–support interactions are challenging to study. Here, it is demonstrated how the combination of the monolayer-controlled formation using atomic layer deposition (ALD) and colloidal nanocrystal synthesis methods leads to catalysts with sub-nanometer precision of active and support phases, thus allowing for the study of the metal–support interactions in detail. The use of this approach in developing a fundamental understanding of support effects in Pd-catalyzed methane combustion is demonstrated. Uniform Pd nanocrystals are deposited onto Al_2O_3/SiO_2 spherical supports prepared with control over morphology and Al_2O_3 layer thicknesses ranging from sub-monolayer to a ≈ 4 nm thick uniform coating. Dramatic changes in catalytic activity depending on the coverage and structure of Al_2O_3 situated at the Pd/Al_2O_3 interface are observed, with even a single monolayer of alumina contributing an order of magnitude increase in reaction rate. By building the Pd/Al_2O_3 interface up layer-by-layer and using uniform Pd nanocrystals, this work demonstrates the importance of controlled and tunable materials in determining metal–support interactions and catalyst activity.

Introduction

Most industrially relevant powder catalysts take advantage of multiple, intimately mixed "active" and "supporting" metal and metal oxide phases to achieve increased catalytic activity, selectivity, or stability. The synergy between supported metal and metal oxide support phases is critical to many important catalytic reactions, ranging from methanol synthesis to ammonia synthesis, and these interactions can influence reaction rates by several orders of magnitude.[1,2] The study of interactions between active and supporting phases, a set of phenomena known as metal-support interactions, is a key area in heterogeneous catalysis, and represents one potential area to modulate and improve catalytic activity.[3,4] Many works have focused on optimizing the "catalyst support effect" in an attempt to find the optimal catalyst support.[5] Although researchers often agree which catalyst support is the most active for a given reaction, the promotional nature of the catalyst support interaction is often unknown. The reactivity of an active phase can be influenced by various interactions with the surface or bulk properties of the support, such as charge transfer, mobility of adsorbate species, generation of unique interface sites, changed nanocrystal morphology or chemical composition, or direct coverage of the active phase with the supporting oxide through strong metal-support interactions (SMSI).[3,6–13]

Often, the fundamental atomic level understanding of metal-support interactions is limited due to the difficulty of synthesizing catalysts with well-defined structures. Recently, many systematic works have emerged which utilize colloidal nanocrystal synthesis to form catalytically active phases, an approach which ensures more direct comparison of the metal-support interactions between a uniform active phase and different supporting materials.[14] Colloidal synthesis permits researchers to deposit the same active phase on different supports, allowing for direct observation of the catalyst support effect. These approaches have yielded success in identifying specific active sites, as well as differences in metal-support interactions for various chemical reactions.[5,8,10,15,16] However, even with uniform colloidal active phases, metal-support interactions may differ based on the support's specific morphology and pore-structure, which can impact the geometric nature of the metal-support interface, as well as transport phenomena within the catalyst bed at elevated reaction rates. Furthermore, although these approaches allow one to probe catalytic activity with distinct supports, it is challenging to draw smooth trends from one support to another due to large differences between the chemistry and crystallinity of different

supporting oxides. Atomic layer deposition (ALD) has emerged as a powerful tool in the study of fundamental catalyst properties and offers a method to address the challenge of comparing catalysts across supports with different compositions, crystallinities, and nanoscale morphologies. In catalyst development, ALD can be used to deposit an overcoat to prevent catalyst deactivation, modify catalyst surface reactivity, or directly fabricate the catalyst active phase with specific desired nanostructures.[17–20] In designing a catalyst support, ALD offers the opportunity to change the surface chemistry of the support, using the underlying material as a template that defines the support morphology.[21–23] By varying the number of ALD cycles, different support surface structures can be obtained with sub-monolayer control over the thickness of the deposited material and allow one to observe the effect of surface and bulk support properties on catalytic reactivity. Furthermore, the conformal nature of ALD films allows different materials to be deposited on identical support templates, thereby decoupling support material from support nanostructure. Combining the controlled active phase synthesis by colloidal methods with the tunable support chemistries and morphologies by ALD enables a high degree of control over all chemical and structural properties of a catalyst.

The ability to synthesize nanomaterials with highly controlled structures and compositions is extremely valuable for the study of a variety of catalysts. In this work we utilize Pd-based methane combustion catalysts to showcase the opportunities available using this combined colloidal-ALD synthesis approach. Pd-catalyzed emissions-control reactions are an important class of reactions which help limit emission of harmful hydrocarbons and pollutants into the environment.[24] Among these reactions, Pd-catalyzed methane combustion to carbon dioxide and water is an important emissions control reaction, and helps mitigate the harmful effects of direct methane emission in the atmosphere.[25,26] The reactivity of Pd strongly depends on the chemical composition of the supporting material.[27] Studies have shown that crystal and morphological support properties can further impact reactivity, even for a single support material. For instance, different researchers have reported that Al_2O_3 supports with varied crystal phases maximize Pd-catalyzed methane combustion activity, citing effects of oxygen mobility in the support, impact of the support on nanocrystal shape and exposed area of PdO phase, and H_2O accumulation on support surfaces.[5,28,29] Some of these differing conclusions may be explained by considering the strong dependence of metal-support interaction on synthesized nanocrystal size and oxidation

state, and the difficulty in designing comparable composite materials with identical active phase and support structure. Therefore, more detailed insights into the Pd-support interactions are necessary to fully understand catalytic performance and instruct researchers on which factors to consider when designing catalysts.

In this study, we combine colloidal nanocrystals and atomic layer deposition processes to precisely control the structure of active and supporting phases in $Pd/X-Al_2O_3/SiO_2$ catalysts (X = number of atomic layer deposition cycles) and understand the metal-support interaction role in the methane combustion emissions control reaction. In this model system, Pd/PdO serves as the catalytic active phase, and we study the transition between pure SiO_2 and Al_2O_3 supporting oxide phases. As SiO_2 provides low rates of the reaction, we can observe the catalytic activity of Pd/Al_2O_3 develop layer-by-layer as we increase Al_2O_3 coverage from sub-monolayer to multiple nanometers in thickness. At low Al_2O_3 coverages below a full monolayer, we see rapid growth in activity as catalytic rates are proportional to Al_2O_3 coverage. At higher ALD cycle numbers, we observe further increased catalytic activity, resulting from bulk structural changes of the Al_2O_3. Additionally, we observe reactivity effects from SiO_2 diffusion into Al_2O_3, showing that support composition plays an important role in determining reaction rate. Overall, this work demonstrates that both extrinsic support properties, such as contact area between metal and support, as well as intrinsic support properties, such as crystalline phase and doping, have important contributions in defining a metal-support interaction and specific catalytic activity.

Experimental

Material Synthesis

Uniform, 8.0 nm colloidal Pd nanocrystals (NCs) were synthesized according to prior work.[30] A single batch of 18 g of SiO_2 spheres were synthesized via a modified Stöber process,[31] according to prior reports,[32] and dispersed into ~500 mL of water. For catalyst synthesis, ~2 g of the supporting SiO_2 spheres were first collected via centrifugation from part of the solution at 8000 rpm for 10 min. At this point, the pellet was dried at 80 °C overnight, and then sieved to produce a fine powder. This powder was then calcined at 600 °C for 24 h (3 ℃ min^{-1} heating and cooling ramp rate) and sieved again in preparation for atomic layer deposition (see below for ALD

details). After atomic layer deposition, the powder was collected again and calcined for 24 h at 900 °C (3 °C min^{-1} heating and cooling ramp rate). Next, an amount of ALD-Al$_2$O$_3$/SiO$_2$ was dispersed in a 7% EtOH/toluene solution and sonicated until the powder was well dispersed. At this point, a diluted solution of Pd NCs was added, and the black dispersion was stirred for 5 minutes to ensure particle deposition on the supports. Finally, the stir bar was removed, and the dispersion was centrifuged at 8000 rpm for 10 min, the colorless supernatant was decanted, and the dark solid was collected. To ensure equal Pd loading across samples, each ALD-Al$_2$O$_3$/SiO$_2$ sample was impregnated with Pd NCs from the same batch at the same time, with the same volume and concentration of Pd/toluene solution. Finally, samples were dried at 80 °C overnight and collected for catalytic measurements and characterization.

Atomic Layer Deposition

ALD was performed in a commercial Gemstar reactor (Arradiance). Powders were held in a stainless steel dish with a stainless steel mesh lid during the depositions.[33] For each deposition, ~250 mg of SiO$_2$ powder was dusted onto the dish through a 180 μm sieve to ensure the support powder was well separated and all surfaces were exposed to the precursors. The samples were pretreated in ozone for 5 minutes prior to deposition to clean and functionalize the surface. Al$_2$O$_3$ was deposited at 250 °C using trimethylaluminum (TMA) and water precursors. In each ALD cycle, the surface was exposed to TMA (pulse time = 0.1 s, soak time = 60 s, purge time = 180 s) and H$_2$O (pulse time = 0.1 s, soak time = 60 s, purge time = 180 s). For each deposition, a Si wafer was placed in the chamber to act as a reference for Al$_2$O$_3$ deposition rate. The thickness of Al$_2$O$_3$ deposited on the Si wafer was measured by spectroscopic ellipsometry and used to confirm a consistent and reasonable Al$_2$O$_3$ growth rate across all depositions.

Catalyst Testing

Catalysts were tested for methane combustion reactivity (CH$_4$ + 2O$_2$ → CO$_2$ + 2H$_2$O) in the presence of H$_2$O. For all experiments, the reaction mixture consisted of 0.5 mol % CH$_4$, 4.0 mol % O$_2$, 3.8 mol % H$_2$O (steam), with the balance Ar. All reactions were performed at atmospheric pressure. Two types of measurements were performed: steady-state, and transient ignition-extinction (light-off) curves. In both cases, 20 mg catalyst was mixed with 380 mg SiC diluent to

prevent hot spots and mass transport limitations. This 400 mg mixture was loaded into a quartz U-tube reactor in between two layers of granular quartz to prevent displacement of the powder catalyst and to preheat the gases before contact with the reactor bed. For reactor heating, the U-tube was placed within a heated square box furnace (Micromeritics). A K-type thermocouple was inserted directly into the catalyst bed to measure the temperature. At the start of any catalytic test, the catalyst was pretreated in 45 mL min^{-1} 5% O_2/Ar for 30 min at 400 °C to burn off any organic components from the catalyst synthesis, and convert Pd into the PdO phase, to avoid any confounding effects of active phase oxidation state in the catalytic analysis. Next, in each experiment, the catalyst was ramped down to 200 °C in 45 mL min^{-1} 5% O_2/Ar. Subsequently, the reaction gas mixture was passed over the reactor bed and the detector stabilized after a few minutes. Finally, the specific temperature program was started according to the specific type of experiment. For ignition-extinction curves, the catalyst was ramped up to 600 °C and back down to 200 °C at 10 °C min^{-1}. The temperature at which 50% methane combustion was achieved (T_{50}) was used as a metric to compare catalyst performance for the ignition-extinction experiments, with lower T_{50} indicating more active catalysts. This measurement was taken with an online mass spectrometer (Hiden HPR-20). For steady-state kinetic testing, the catalyst was ramped to a specific temperature at 10 °C min^{-1}, which was held until steady-state CH_4 conversion was obtained. This measurement was performed at four temperature points, and only stable kinetic points were used for analysis. An online gas chromatograph (GC, Buck Scientific Model 910) equipped with a flame ionization detector (FID) and thermal conductivity detector (TCD) was used for quantification of the reactants and products, which were then used to calculate reaction rates by normalizing by the amount of Pd or total catalyst mass given that no differences in Pd surface area are expected when using the same Pd nanoparticles for all the samples.

Microscopy Characterization

Transmission electron microscopy (TEM) images were acquired on a FEI Tecnai TEM operating at 200 kV accelerating voltage equipped with an Orius CCD. Electron diffractograms were also acquired on a Tecnai operating in STEM mode. For diffraction imaging, the full diffractogram was first observed on the viewing window, and the objective aperture was used to select a diffracted beam as the imaging beam to produce the diffraction dark-field images. High angle

annular dark field scanning transmission electron microscopy (HAADF-STEM) images and spatially resolved energy dispersive spectroscopy maps (EDS-mapping) were acquired on a FEI TitanX operating at 300 kV at the National Center for Electron Microscopy (NCEM) at the Lawrence Berkeley National Laboratory (LBNL). EDS-maps were acquired on the TitanX equipped with a SuperEDS detector consisting of four window-less silicon drift detectors with a collection solid angle of 0.7 steradians. Map acquisition was typically < 5 min at a beam current of 330 pA. For Al/Si statistical quantification of single catalytic nanospheres, EDS was performed by focusing the TEM probe over a single particle using a single EDS detector on an FEI Tecnai. For sample preparation, powder samples were dispersed on lacey C/Cu grids by shaking a small amount of powder sample with a TEM grid in a small scintillation vial. Particle size was measured using ImageJ software. Elemental maps were analyzed using ESPIRT 1.9 software.

X-ray Photoelectron Spectroscopy

X-ray photoelectron spectroscopy (XPS) was performed with a PHI VersaProbe 3 using Al Kα radiation (1486.6 eV). Powder samples were deposited onto conductive carbon tape on top of an Al holder, which was outgassed at 10^{-2} Pa before inserted into an ion-pumped analysis chamber which was held at ~$5x10^{-7}$ Pa throughout analysis. For all samples, an excitation of 100 W at 20 kV with a pass energy of 55 eV were used. The beam spot size was 100 μm for all samples, and an Ar^+ neutralizer and an electron flood gun were used to minimize sample charging. Binding energies were all referenced to the C1s peak at 284.8 eV.

X-ray Diffraction (XRD)

A Bruker Single Crystal D8 Venture with Cu Kα radiation (λ = 1.5406 Å) was used to collect X-ray diffractograms. The powder was loaded into a thin quartz tube, which was rotated on the z-axis through diffractogram collection. The diffracted beams were collected across 10º to 90º 2θ angles with a step size of 0.05º and an exposure time of 150 s. Diffraction rings were integrated to produce 1-dimensional diffraction patterns.

Inductively Coupled Plasma Atomic Emission Spectroscopy (ICP-OES)

Although the same amount of Pd was deposited onto all samples, as all Pd NCs came from the same colloidal solution, Pd quantification for each catalyst was performed using ICP-OES on the supported catalysts to control for small Pd differences between catalysts. Quantitative Pd analysis was performed on an ICP-OES instrument (Thermo Scientific ICAP 6300 Duo View Spectrometer). ~15 mg catalyst powder was digested in a mixture of nitric acid (710 µL) and hydrochloric acid (660 µL) in a borosilicate test tube, which was sonicated every two hours. This mixture was then filtered, the supernatant collected, diluted to ~5 ppm Pd, and then measurements were taken.

Thermogravimetric Analysis

Thermogravimetric analysis (TGA) measurements were performed on colloidal Pd and SiO_2 solutions to determine concentrations of each solid nanoparticle within their respective solution. For each measurement, ~150 µL of solution was slowly evaporated into a tared, small aluminum crucible using a hot plate. Next, this crucible was loaded into the TGA which was headed to 500 °C at 45 °C min^{-1}, and then held until a stable mass was reached. By dividing this mass into the original solution volume, a concentration was measured for a given solution. Concentrations of Pd NCs were generally ~10mg mL^{-1}, and for SiO_2 spheres ~40 mg mL^{-1}.

Infrared (IR) Spectroscopy

IR measurements were performed in a Thermo Fisher iS50 spectrometer. Measurements were performed on the supports that had been calcined at 900 °C in air and subsequently were stored at room temperature in air for ~1 week. For each measurement, 5-7 mg of sample was pressed into a 7 mm die set to form a self-supported wafer. The IR measurement chamber was purged with N_2 for 15 minutes prior to each measurement to remove CO_2 and H_2O vapors. Background spectra were measured with an empty chamber, purged with N_2 for 15 minutes. IR spectra were collected at 4 cm^{-1} resolution, averaged over 128 scans, and measured by a deuterated lanthanum α-alanine doped triglycine sulfate (DLaTGS) detector. Spectra were baseline-corrected in the O-H stretch and Si-O-Si backbone overtone vibration regions. The area of the Si-O-Si backbone overtone features was calculated by integrating the baseline-corrected spectra. The O-H region

was deconvoluted into two components for each spectrum. No other components were needed to accurately model the O-H stretching feature.

^{27}Al Solid State Nuclear Magnetic Resonance (NMR) Spectroscopy

All NMR data were collected with a Varian Inova 600 spectrometer (14.1 T field, 156.25 MHz for ^{27}Al), using a Varian "T3" probe with a 3.2 mm, low-Al zirconia rotor spinning at 20 kHz. Spectra were referenced to 0.1 M aqueous $Al(NO_3)_3$ at 0 ppm. Radiofrequency power was about 100 kHz; single pulse acquisition was used with 0.2 ms pulses, corresponding to a radiofrequency tip angle of about 20˚ for solids with significant quadrupolar coupling. Relatively short relaxation delays of 0.1 s between pulses allowed averaging of as many as 1.5×10^6 acquisitions, yielding useful signal to noise ratios even for materials with low Al contents. Data collected on selected samples with delays of 1 and 10 s showed that relaxation was at least 90% complete at 0.1 s, and that differential relaxation among signals for different Al sites was negligible.

^{27}Al rotor background (comprising a maximum of about 5-10% of observed intensity) was subtracted from the spectra for the low-Al samples using data collected for the empty rotor. Rough total signal intensities were estimated simply by integrating the central peaks in the spectra, without correcting for spinning sidebands. Given that most spectra had very similar lineshapes (and thus similar distributions of Al species and quadrupolar parameters), these integrals provide useful relative comparisons of observable Al content. Bulk amorphous alumina was prepared by slowly heating $Al(NO_3)_3$-$9H_2O$ reagent to 510 ˚C and annealing at that temperature for 27 h. This material was X-ray amorphous and contained about 5 wt. % residual H_2O based on weight loss on heating to 1000 ˚C and conversion to the α-phase. Heating of the amorphous alumina to 800 ˚C for 2 h converted it to a 'transition' alumina that is probably the γ-phase.

Results and Discussion

Model Pd/Al$_2$O$_3$/SiO$_2$ Catalyst Synthesis Through Combined ALD and Colloidal Method

The aim of this work is to gain new insights into the nature of catalyst metal-support interactions by synthesizing model catalysts with precise control over the geometric and chemical properties of the metal-support interface. In this work, our catalyst building blocks were colloidally synthesized uniform 8.0 nm Pd nanocrystals (NCs) and purchased $\approx$ 200 nm amorphous Stöber SiO_2 spheres. In traditional catalyst synthesis through wet or incipient impregnation techniques, catalyst morphology and oxidation state are strongly coupled to the support properties on which the active phase is being deposited or impregnated. However, by starting with highly uniform, preformed Pd NCs, we ensure that our NC active phases should be nearly identical across different catalyst supports.[14] Additionally, the use of relatively small diameter SiO_2 spheres as our base support helps ensure uniform ALD coverage due to limited numbers of inaccessible pores.[34,35] Our specific Stöber SiO_2 support geometry was also chosen for ease of characterization, so we can readily characterize ALD coverage at the nanoscale (a more difficult challenge with other highly-porous catalyst supports). SiO_2 was also chosen as the base support due to its relative inertness for various types of chemical interactions with supported phases, and because Pd/SiO_2 catalysts show relatively low rates for the reaction of interest.[36]

For methane oxidation, Pd/SiO_2 has poor reactivity, while Pd/Al_2O_3 is well-established and industrially utilized.[37,38] To understand what properties of the support lead to promoted activity, we build a Pd/Al_2O_3 catalyst up from a SiO_2 support, layer-by-layer. The SiO_2 spheres were coated with different thicknesses of Al_2O_3 by ALD (0 - 40 cycles, 0 - 4.8 nm).The Al_2O_3 growth rate was measured to be approximately linear on a Si wafer, at a rate of 1.1 Å per cycle, which is reasonable for ALD Al_2O_3 (**Figure S1**).[39] After the alumina coating, the powder was calcined at 900 ℃ for 24 h to ensure stability of the film during the subsequent catalytic testing conditions at temperatures up to 600 ℃. At this point, colloidal Pd nanocrystals were deposited on the support surface. A schematic of the catalyst synthesis is shown in **Figure 1**.
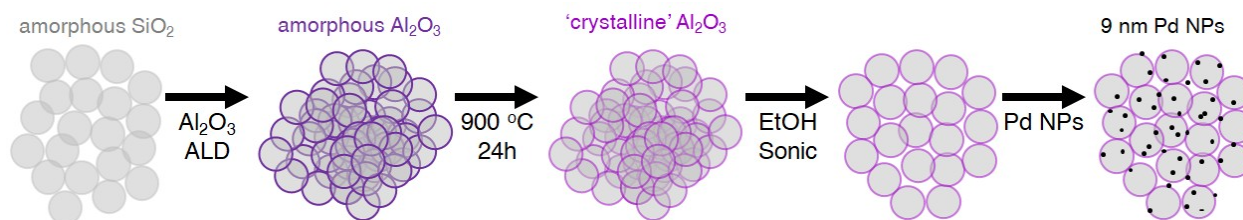
Figure 1. Procedure used to synthesize Pd/ALD-Al$_2$O$_3$/SiO$_2$ catalysts with tunable support thickness and controlled nanocrystal size and loading.

Representative transmission electron microscopy (TEM) images of selected catalysts are shown in **Figure 2**. Going from Pd/1-Al$_2$O$_3$/SiO$_2$ to Pd/40-Al$_2$O$_3$/SiO$_2$, we observe a distinct increase in the thickness of the Al$_2$O$_3$ surface. At 1 and 3 ALD cycles, the Al$_2$O$_3$ is too thin to be clearly observable in the images, but at 20 and 40 ALD cycles a distinct conformal overcoat is visible as a slightly darker border around the silica spheres. The shell thickness can be best observed at higher resolution in **Figure S2**. Importantly, we observe that Pd NCs are randomly deposited onto the surface of each sample, and that the NCs are uniform in size across catalysts, as expected since they were prepared using the same starting Pd nanocrystals (**Figure S3**). Therefore, this system achieves controlled support geometry and active phase, and singly varies the effect of support properties, in the form of coverage and thickness, on catalytic behavior.
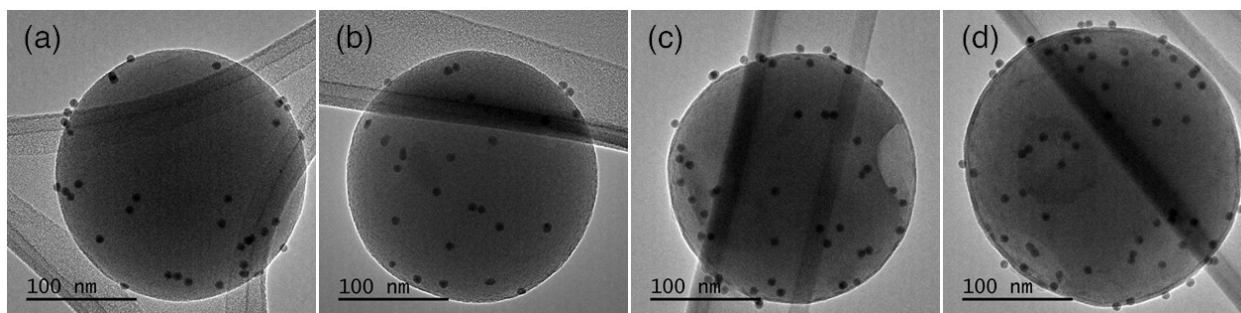

Figure 2. Transmission electron microscopy (TEM) images of Pd/ALD-Al$_2$O$_3$/SiO$_2$ catalysts with (a) 1 ALD cycle, (b) 3 ALD cycles, (c) 20 ALD cycles, and (d) 40 ALD cycles.

We use energy-dispersive x-ray spectroscopy (EDS) to quantify and characterize the uniformity of Al$_2$O$_3$ deposition on individual SiO$_2$ spheres as well as across SiO$_2$ spheres. Qualitatively, we observe that for Pd/5-Al$_2$O$_3$/SiO$_2$, Pd/10-Al$_2$O$_3$/SiO$_2$, and Pd/40-Al$_2$O$_3$/SiO$_2$, each SiO$_2$ sphere is completely coated with Al$_2$O$_3$ (**Figure 3,** see Figure SX for spectrum from 3c showing the edges). Furthermore, we observe increased Al signal, especially at the outer edges of the spheres, as we increase the ALD deposition from 5-cycles to 10-cycles. For more quantitative characterization, we performed single-sphere compositional analysis for Al concentration for the

Pd/40-Al$_2$O$_3$/SiO$_2$ sample (**Figure S4**). We observe ~20 at. % Al (80 at. % Si) within 95% of the spheres in these catalysts, suggesting that our entire sample is uniformly coated with the same amount of Al across all spheres. Overall, elemental analysis shows the uniformity of our catalysts at the nanoscale and provides evidence that we successfully created samples with monodisperse Pd nanocrystals on conformal, thickness-controlled ALD Al$_2$O$_3$ coated SiO$_2$ nanospheres.
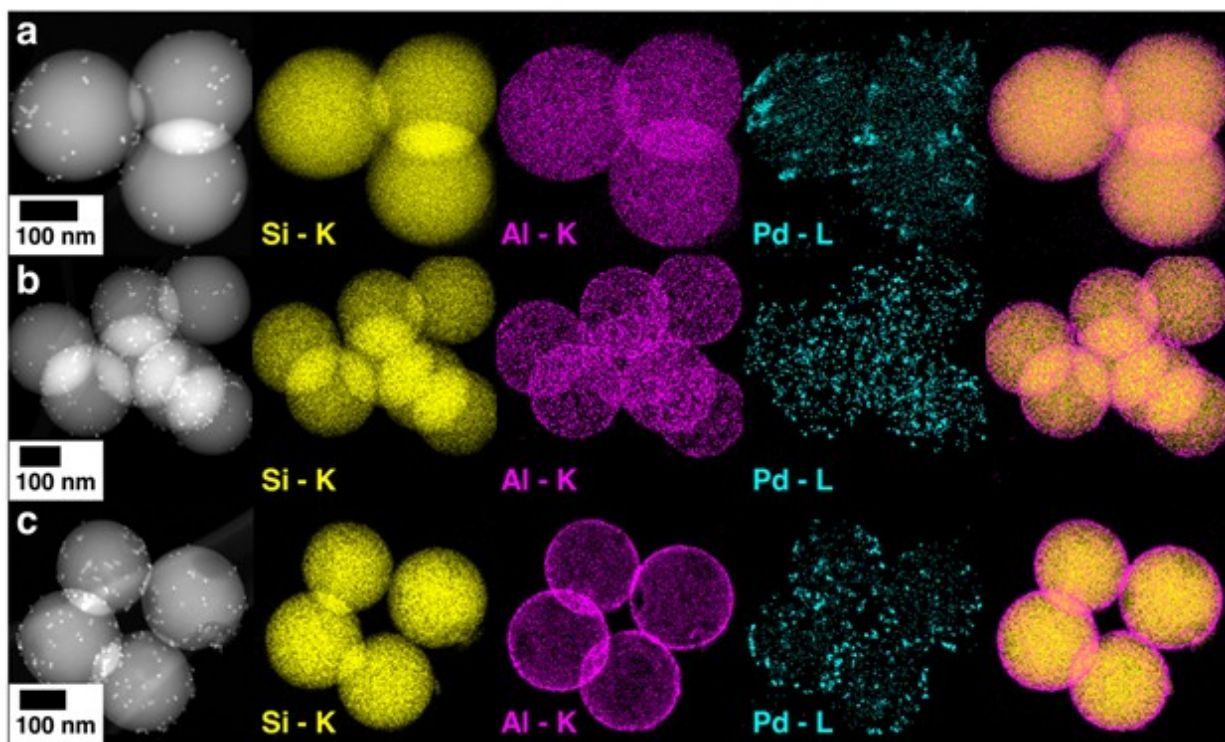

Figure 3. STEM-EDS elemental maps of Pd/ALD-Al$_2$O$_3$/SiO$_2$ catalysts. Panels from left to right show HAADF-STEM image, Si map, Al map, Pd map, and superimposed Si and Al maps. (a) Pd/5-Al$_2$O$_3$/SiO$_2$, (b) Pd/10-Al$_2$O$_3$/SiO$_2$, (c) Pd/40-Al$_2$O$_3$/SiO$_2$.

The Effect of Al$_2$O$_3$ Support Modification on Pd-Catalyzed Methane Combustion

The eight Pd/ALD-Al$_2$O$_3$/SiO$_2$ catalysts, in addition to a Pd/γ-Al$_2$O$_3$ control catalyst synthesized from commercial Al$_2$O$_3$, were tested for methane combustion activity in the presence of steam. For this reaction, all catalysts were pre-oxidized *in-situ* at 400 °C to begin testing with a PdO active phase and burn off any residual organic components from the colloidal synthesis. Steady-

state kinetic measurements show a clear difference in catalytic rate as a function of number of ALD cycles (**Figure 4a**). The catalysts show activation energies ranging from 125 to 162 kJ mol^{-1}, which is in a similar range as previously reported,[5] with no clear trend. When the catalytic rate is linearly extrapolated to 350 °C, a factor of ~27 difference between rates is observed across the various thicknesses of the Al_2O_3 coating (**Figure 4b**). As Al_2O_3 thickness increases, we observe two regimes of improved reactivity. From 0 to 3 ALD cycles, the reaction rate increases linearly with ALD cycle number. From 5 to 40 ALD cycles, the reaction rate continues to increase linearly, but with a slower dependence on ALD cycle number. As the Pd NCs and the support morphology are identical across catalysts, this large difference in catalytic rate can only be attributed to the interaction between the Pd/PdO active phase and the amount and structure of Al_2O_3 at the Pd/Al_2O_3 interface. Post-catalysis TEM shows the stability of the Pd NCs and Al_2O_3 film to the reaction conditions, showing no significant NC sintering or peeling of the Al_2O_3 ALD film (**Figure S5**).
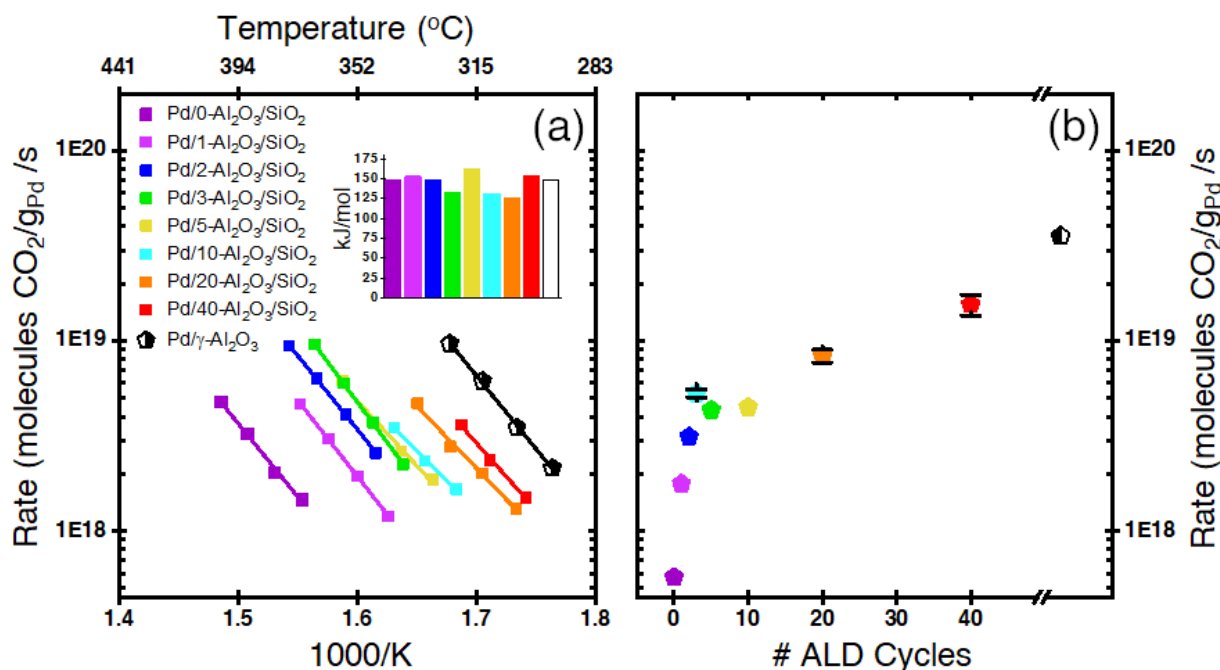

Figure 4. Steady-state methane combustion activity of Pd/ALD-Al_2O_3/SiO_2 catalysts and a comparison Pd/γ-Al_2O_3 in the presence of steam. (a) Kinetic measurements conducted in 0.5 mol % CH_4, 4.0 mol % O_2, 3.8 mol % H_2O. Inset shows activation barriers measured from the slope in the Arrhenius plot. (b) Extrapolated steady-state rate of methane combustion at 350 °C. For

points with error bars, error bars represent the widest range of activity between experiments, and the point represents the average activity of those points.

In transient ignition-extinction experiments for the same reaction, we observe a similar ordering of catalytic activity across samples, and a ~104 °C difference in the temperature for 50% conversion (T_{50}) between the Pd/SiO_2 and the $Pd/40-Al_2O_3/SiO_2$ samples (**Figure S6**). Importantly, we observe that in both sets of experiments, more cycles of Al_2O_3 deposited leads to significantly increasing catalytic activity, although the change in activity is not proportional to the mass of Al_2O_3 deposited across the whole range investigated here. As with the kinetic measurements, we observe a large increase in activity across the first three ALD cycles, and a slower but continuously increasing activity from 5 ALD cycles to 40 ALD cycles. However, although our catalysts show an increase in reactivity 27 times that of the Pd/SiO_2, the $Pd/40-Al_2O_3/SiO_2$ still shows activity less than the $Pd/\gamma-Al_2O_3$ control catalyst by a factor of ~2.3. This data suggests that although the ALD-derived samples are asymptotically approaching the bulk Al_2O_3 support through ALD layers, there are still chemical or structural differences between the synthetic materials and high surface area Al_2O_3.

Bulk Properties Governing the Pd-Support Interaction

The two regimes of improved catalytic performance as a function of Al_2O_3 thickness indicate that multiple factors contribute to the Pd-support interaction. The surface chemistry of the support can impact catalytic performance due to differences in chemical properties between Si and Al. This effect would be manifested through the relative fraction of Pd-Si and Pd-Al interface sites. The Pd-support interaction can also be influenced by bulk properties of the support. The electronic structure of the support surface depends on the crystal structure and chemical composition of the bulk material. To better understand the Pd-support interactions, the bulk and surface properties of the support were characterized and related to the catalytic performance.

To identify the bulk crystal structures of the supporting oxide, the $ALD-Al_2O_3/SiO_2$ supports were characterized by X-ray diffraction (**Figure 5a**). For all samples, no crystalline features attributable to the SiO_2 can be detected, as expected for amorphous SiO_2 prepared by the Stöber process.[40] For the supports with 10 or fewer Al_2O_3 ALD cycles, no crystalline features from the

Al_2O_3 films are detected in the XRD pattern. The lack of diffraction peaks in the XRD patterns indicates that the Al_2O_3 is either amorphous, contains very low concentrations of crystalline Al_2O_3, or possesses crystallites too small to detect by XRD. For these low ALD cycle numbers in particular, the Al_2O_3 layers are thinner than 1.2 nm, likely below the size detection limit of XRD.[41] For the 20-Al_2O_3/SiO_2 sample, peaks attributed to γ-Al_2O_3 emerge, but the diffraction peaks in this sample are still very weak. In the 40-Al_2O_3/SiO_2 sample, these diffraction peaks grow in intensity, confirming the presence of γ-Al_2O_3 at a sufficiently thick layer of Al_2O_3. The crystallite size estimated from the Scherrer equation is 5.2 nm, comparable to the 4.8 nm film thickness measured by TEM, suggesting that all the Al_2O_3 is in the γ phase.
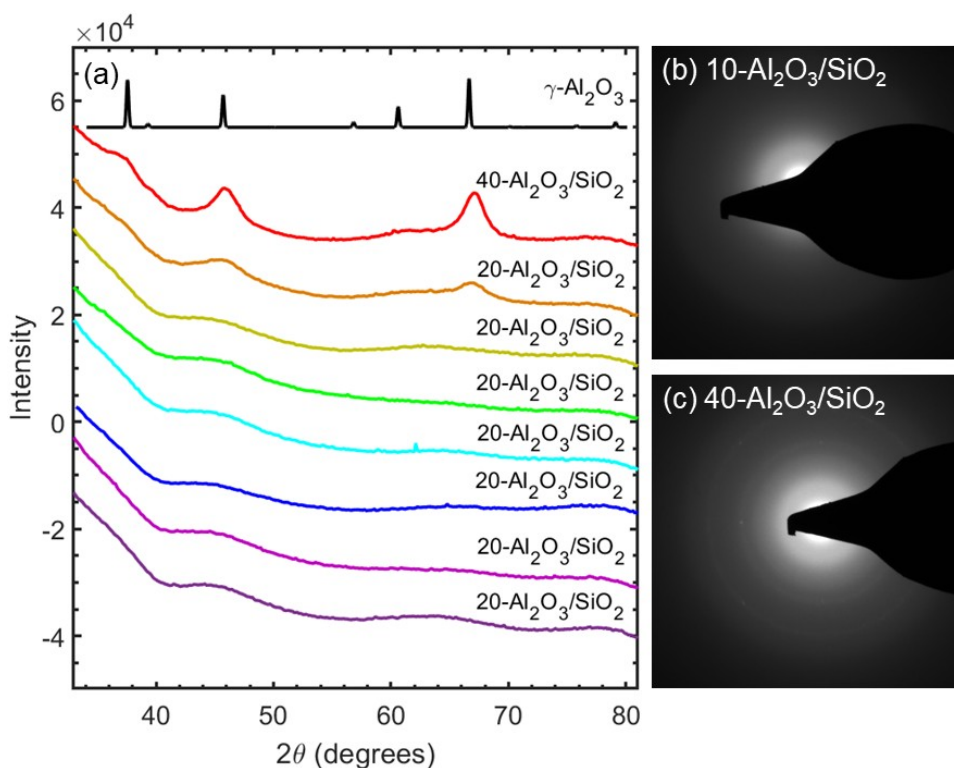

Figure 5. (a) XRD patterns of Pd/ALD-Al_2O_3/SiO_2 catalysts. Standard pattern for γ-Al_2O_3 provided for reference. Electron diffraction patterns for (b) 10-Al_2O_3/SiO_2 and (c) 40-Al_2O_3/SiO_2 supports.

Electron diffraction and STEM imaging were also performed to characterize the crystal structure of the Al_2O_3 films for 10 or fewer ALD cycles. Electron diffraction allows for small crystallites

to be spatially resolved.[42] No electron diffraction is observed for the 10-Al_2O_3/SiO_2 sample, whereas diffraction rings are present in the 40-Al_2O_3/SiO_2 sample (**Figure 5b,c**). This result supports the XRD measurement, showing no crystalline features for 10 or fewer ALD cycles. The presence of γ-Al_2O_3 is further confirmed by STEM-imaging (**Figure S7**). Crystallites are observed in the samples with 20 and 40 Al_2O_3 ALD cycles, but not for the 10-Al_2O_3/SiO_2 sample. Previous studies of Al_2O_3 ALD have shown that the as-deposited films are amorphous.[43,44] Thus, the formation of γ-Al_2O_3 is promoted by the 900 ℃ calcination pretreatment, with the additional condition that the Al_2O_3 film must be thick enough to form crystalline domains.

The formation of γ-Al_2O_3 at high ALD cycle numbers potentially impacts the Pd-support interaction and the resulting catalytic performance. Therefore, another experiment was conducted to directly determine the effects of Al_2O_3 crystallization on catalytic activity. 40 cycles of Al_2O_3 ALD was performed on the SiO_2 nanospheres. The powder was split into two batches, one of which was calcined at 600 ℃ while the other was calcined at 900 ℃. Pd nanocrystals from a single synthesis batch were then deposited on these supports with identical loading. TEM imaging and electron diffraction were used to confirm that the sample calcined at 600 ℃ remained amorphous while the sample calcined at 900 ℃ formed γ-Al_2O_3, and the Al_2O_3 thickness and Pd loading were identical between these catalysts (**Figure S8**). The kinetics of methane combustion were measured for each of these catalysts (**Figure S9**). The sample calcined at 900 ℃ had a higher reaction rate than the sample calcined at 600 ℃. Thus, the conversion of the Al_2O_3 support from the amorphous phase to the γ phase enhances methane combustion reactivity over Pd. The gradual increase in reaction rate at high Al_2O_3 ALD cycle numbers can therefore be partly explained by the partial crystallization of the 20-Al_2O_3/SiO_2 support and the full crystallization of the 40-Al_2O_3/SiO_2 support. The dependence of Pd activity on Al_2O_3 crystallinity is broadly consistent with claims from previous studies,[45] but the synthesis approach in this work allowed the crystallinity and textural properties of the support to be clearly decoupled.

To better understand the structure of the ALD-Al_2O_3/SiO_2 support at low cycle numbers where no diffraction peaks were observed, the supports were studied by ^{27}Al solid-state NMR spectroscopy (**Figure 6a**). Three main features are present in the NMR spectrum of Al_2O_3, resulting from Al-O bonds in 4-, 5-, and 6-fold coordination environments. For the 1-Al_2O_3/SiO_2

sample, the most prominent species is 4-coordinate Al-O. The high proportion of this under-coordinated species suggests that the Al is present primarily at the surface of the silica spheres as monomeric species, as expected for a single ALD cycle. For the catalysts with 2 through 20 ALD Al_2O_3 cycles, 4-, 5-, and 6-coordinated Al-O species are detected. The presence of Al in each of these coordination environments is characteristic of amorphous Al_2O_3,[46] as can be seen by the comparison of the sample spectra to that of the amorphous Al_2O_3 standard. Furthermore, the relative intensities of these peaks are qualitatively similar to those of the amorphous Al_2O_3 standard. We note that the detection of amorphous Al_2O_3 in the 20-Al_2O_3/SiO_2 sample does not contradict the diffraction measurements discussed above. It is difficult to detect a small amount of γ-Al_2O_3 by NMR in an otherwise amorphous sample due to overlap between the 4- and 6-coordinated Al-O species in the NMR spectra of amorphous and γ-Al_2O_3. Taken together, the NMR and diffraction results indicate that the 20-Al_2O_3/SiO_2 sample contains a mixture of amorphous and γ-Al_2O_3. Finally, the NMR spectrum of the 40-Al_2O_3/SiO_2 sample closely resembles that of the γ-Al_2O_3 standard, with no remaining 5-coordinated Al-O species. As with the diffraction measurements, the NMR data show that the Al_2O_3 film crystallizes to γ-Al_2O_3 when it is sufficiently thick.
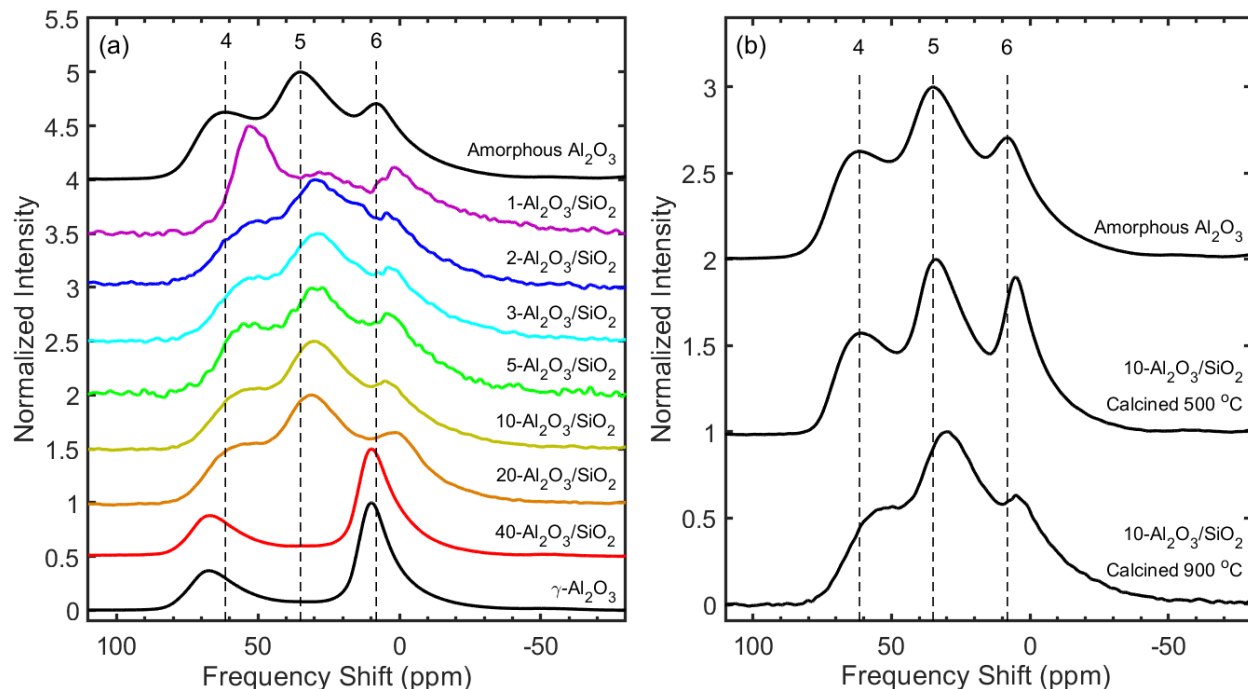
Figure 6. ^{27}Al NMR spectra of (a) 900 ℃ calcined ALD-Al_2O_3/SiO_2 supports and (b) 10-Al_2O_3/SiO_2 calcined at 500 ℃ and 900 ℃. Standard spectra for amorphous and gamma alumina included for reference.

There is one significant discrepancy between the amorphous Al_2O_3 standard NMR spectrum and those of the ALD-Al_2O_3/SiO_2 supports for 20 or fewer ALD cycles. The peaks in the NMR spectra of the catalyst supports are shifted ~5 ppm lower in frequency compared to those of the amorphous Al_2O_3 standard. Such a shift is consistent with Al coordination including Si neighbors,[47] and suggests that intermixing occurs between the ALD Al_2O_3 film and the underlying SiO_2 support. Since Al/Si intermixing is not expected to occur during the ALD process, we hypothesize that it results from the 900 °C calcination of the support. To test this hypothesis the NMR spectra of the 10-Al_2O_3/SiO_2 support calcined at 900 ℃ was compared to a 10-Al_2O_3/SiO_2 sample that was calcined at 500 °C (**Figure 6b**). The peak positions in the NMR spectrum of the sample calcined at 500 °C agree with those of the amorphous Al_2O_3 standard without any shift, indicating that the lower temperature treatment was not sufficient to induce Al/Si intermixing. There is a slight difference in the 6-coordinated peak position between the sample calcined at 500 °C and the amorphous Al_2O_3 standard, suggesting a minor structural difference between the two materials. Finally, to confirm that the shifts in NMR speak positions result from intermixing between Si and Al, rather than some other structural difference between the ALD Al_2O_3 and the amorphous Al_2O_3 standard, a high-resolution STEM-EDS line scan was performed on the 40-Al_2O_3/SiO_2 sample (**Figure S10**). Although the metal at the support surface is primarily Al, a small amount of Si is detected in the Al_2O_3 shell, consistent with some intermixing of these elements. The Si/Al intermixing revealed by the NMR measurements can impact catalytic performance in two ways. First, the mixing of Si into the Al_2O_3 film changes the composition of the support, which can affect the electronic structure of the surface and thus the Pd-support interactions. Second, this intermixing may result in Si at the surface of the support, in direct contact with the Pd nanoparticles. As is apparent from the catalytic measurements, the methane combustion reactivity is very sensitive to the chemical composition of the surface of the support, so the presence of a small amount of Si at the surface would have significant effects on reactivity. The presence of a small amount of Si at the surface of the Pd/40-Al_2O_3/SiO_2 support

may contribute to the lower reaction rate for this catalyst than the Pd/γ-Al$_2$O$_3$ catalyst. Overall, we observe the effect of bulk crystalline changes from amorphous Al$_2$O$_3$ to crystalline Al$_2$O$_3$, as well as changes in the purity of the Al$_2$O$_3$ phase from SiO$_2$ doping, as factors that determine metal-support interactions for Pd-catalyzed methane combustion.

Surface and Interfacial Properties Governing the Pd-Support Interaction

The diffraction and NMR measurements presented in the previous section reveal the bulk composition and crystallinity of the ALD-Al$_2$O$_3$/SiO$_2$ supports. However, they do not provide direct insight into the surface properties of the ALD-Al$_2$O$_3$/SiO$_2$ support, which is particularly important for understanding the Pd-support interactions that result in the rapid linear increase in reaction rate at low cycle numbers. The chemical composition of the ALD-Al$_2$O$_3$/SiO$_2$ support surface was therefore characterized by XPS. As expected, with increasing ALD cycle number, the ratio of Al 2p to Si 2p peak intensities increases (**Figure 7a**). The surface percentage of Al relative to Si, Al/(Al+Si), was computed as a function of ALD cycle number (Figure 7b). At low cycle numbers, the surface fraction of Al increases linearly with the number of ALD cycles. This behavior is consistent with an ideal, layer-by-layer ALD growth process.[48–50] At high cycle numbers, the Al surface percentage continues to increase at a slower rate, and appears to asymptotically approach a purely alumina surface.
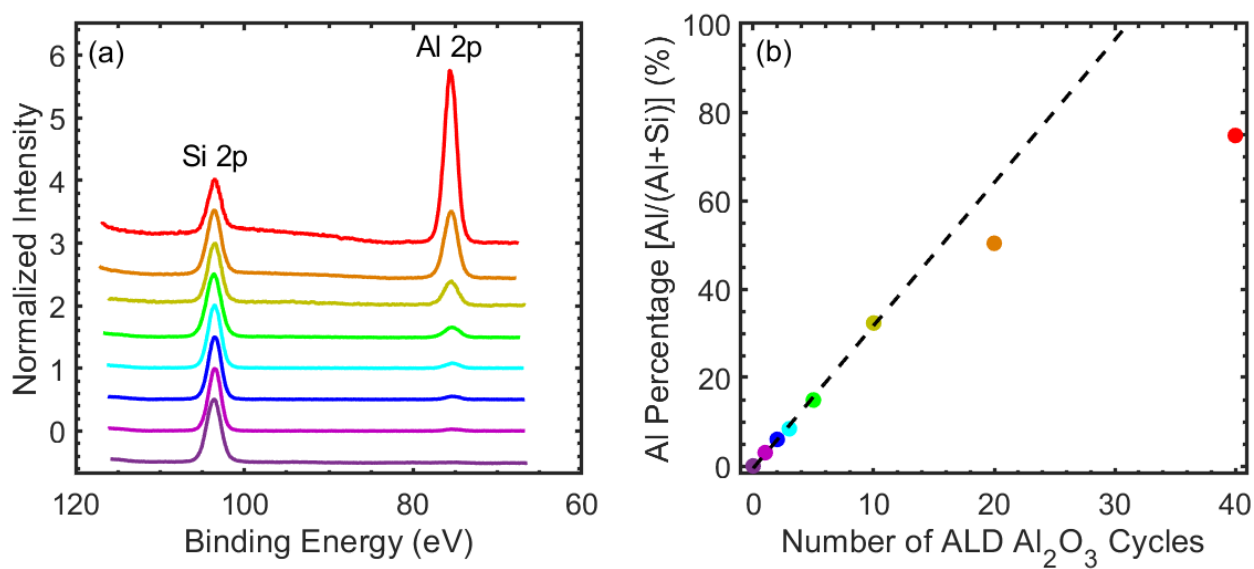
Figure 7. (a) Si 2p and Al 2p regions of the XPS spectrum and (b) surface Al percentage for 900 °C calcined ALD-Al_2O_3/SiO_2 supports as a function of ALD cycles.

Previous studies of ALD Al_2O_3 have shown that under ideal layer-by-layer growth conditions, the amount of material deposited is approximately 0.3 monolayers per cycle.[39] Thus, under ideal growth conditions, as indicated by the linear increase in Al concentration at low cycle numbers measured by XPS, we expect a full monolayer of Al_2O_3 to form over the course of the first ~3 ALD cycles. In the context of the catalytic measurements, the rapid linear increase in reaction rate also occurs during the first 3 ALD cycles. These two observations lead us to hypothesize that during the first three ALD cycles, the Pd-support interaction changes from primarily Pd-SiO_2 to primarily Pd-Al_2O_3, and this change in the chemistry of the metal-support interaction drives the rapid increase in reaction rate.

IR measurements were performed on the ALD-Al_2O_3/SiO_2 supports to understand the change in surface chemistry at low cycle numbers. There are two regions of interest in the IR spectrum. First, the silanols (Si-OH) present in the samples are characterized from the O-H stretch region (Figure S11a).[51,52] Second, an overtone of the Si-O-Si backbone vibration is used to quantify the amount of sample in the IR beam and normalize the data (**Figure S11b**).[53,54] The O-H stretching peak in the IR spectrum of each sample is deconvoluted into two gaussian components. Example deconvolutions are shown in **Figures 8a and 8b**, and the deconvolutions for all samples are shown in **Figure S12**. The peak component at ~3747 cm⁻¹ is assigned to surface silanol Si-OH species, while the broader peak at ~3741 cm⁻¹ is assigned to bulk Si-OH,[55] both of which result from the Stöber synthesis process. The two components are present in the 0-Al_2O_3/SiO_2 support, in which no Al_2O_3 is present, indicating that they both result from Si-bound OH groups. As the Al_2O_3 loading increases, no additional O-H stretching features emerge, demonstrating that no Al-OH species were detected in any samples. The area of the surface Si-OH species (~3747 cm⁻¹) was normalized to the integrated area of the Si-O-Si backbone overtone internal standard, and the results are shown in **Figure 8c**.
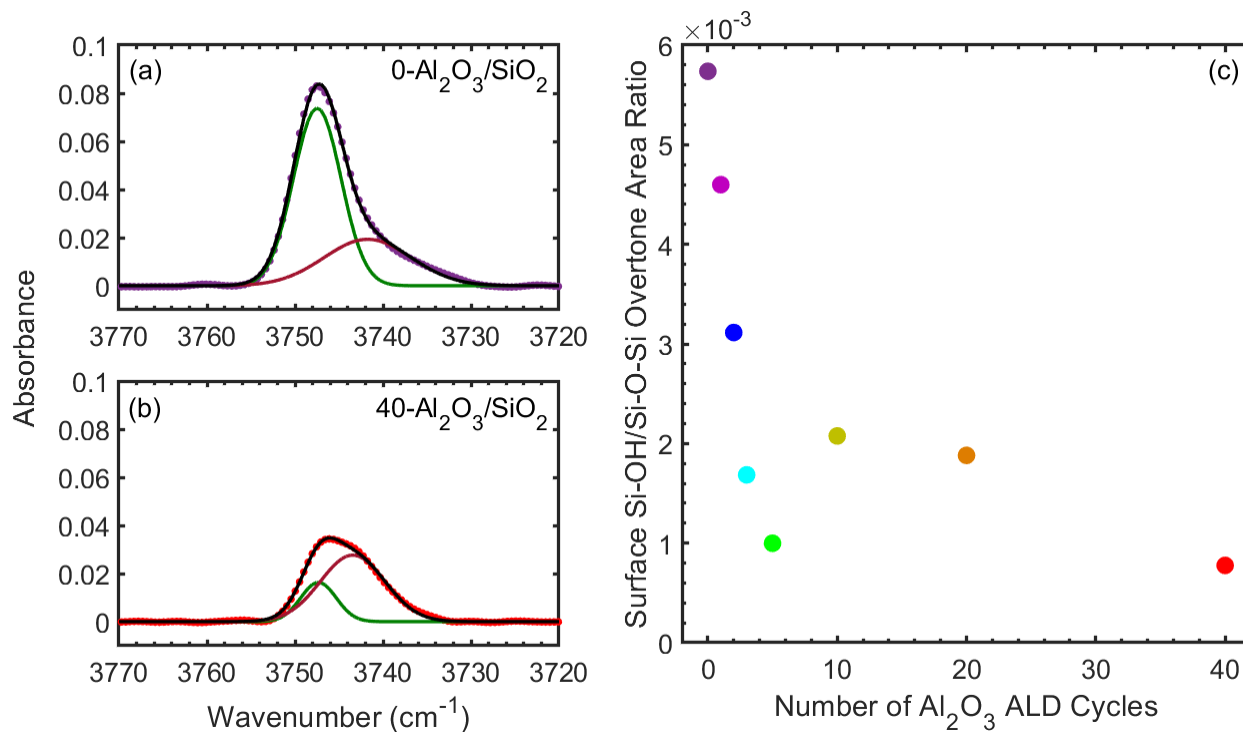
Figure 8. Deconvolution of OH stretch region of the FTIR spectrum plotted on the same scale for (a) 0-Al$_2$O$_3$/SiO$_2$ and (b) 40-Al$_2$O$_3$/SiO$_2$ supports. (c) Area ratio of surface Si-OH to overtone of backbone Si-O-Si vibration measured by FTIR spectroscopy.

The surface Si-OH/Si-O-Si area ratio shows a trend that is in line with the catalytic results as a function of ALD cycle number. Across the first 3 Al$_2$O$_3$ ALD cycles, there is a rapid linear decrease in the surface Si-OH content, resulting from the reaction of surface OH groups with TMA during the ALD process. The decrease in surface Si-OH content does not continue beyond 3 ALD cycles, and the variations in surface Si-OH content from 3 to 40 cycles are believed to be within the error of the measurement. The combination of the catalytic and IR measurements clearly demonstrates that 3 ALD cycles is the threshold for one monolayer of Al$_2$O$_3$ coverage. As the Al$_2$O$_3$ loading increases from 3 to 40 cycles, there are variations in the surface Si-OH/Si-O-Si area ratio, but no clear trend. However, even in the samples with 10 or more Al$_2$O$_3$ ALD cycles, which nominally should have several monolayers of Al$_2$O$_3$ coverage, the surface Si-OH content is not zero. There are two possibilities for this observation. The first is that some of the surface Si-OH groups are inaccessible to the ALD precursors, for instance due to diffusion limitations as have been reported for porous substrates.[34,56] However, since the spherical substrates used here

are non-porous and conformality was confirmed by TEM, all surfaces of the SiO_2 powder are expected to be accessible. The more likely explanation for the presence of surface Si-OH at high ALD cycle numbers is due to the Si/Al intermixing revealed by NMR, which would bring some Si atoms to the surface of the ALD-Al_2O_3/SiO_2 supports. Finally, we note that the area ratio of the ~3741 cm^{-1} O-H stretch peak to that of the Si-O-Si backbone overtone shows no trend and relatively small variation with Al_2O_3 coverage, supporting the assignment of this peak as bulk Si-OH species (**Figure S13**). We propose that the presence of Si at the surface of the ALD-Al_2O_3/SiO_2 supports alters the Pd-support interaction and consequently affects the methane combustion rate. From the reaction rates measured at low ALD cycle numbers, it is clear that the activity of Pd is extremely sensitive to the chemical composition of the support surface, so small amounts of surface Si, even with several monolayers of Al_2O_3, would be expected to significantly impact reactivity.

Having characterized the properties of the ALD-Al_2O_3/SiO_2 support, we can now understand how the support structure and Pd-support interactions give rise to the catalytic behavior presented in **Figure 4**. The catalyst structure and Pd-support interactions are visualized in **Figure 9**. First, the interfacial chemistry between the Pd and the support has a significant effect on the reaction rate, due to the much higher reactivity of Al_2O_3-supported Pd compared to SiO_2-supported Pd. The chemical composition of the support surface, in particular the Al:Si ratio, is determined by the amount of Al_2O_3 deposited and the intermixing between the Al_2O_3 film and the underlying SiO_2. We describe the following model to explain the results with ALD cycle number. At low cycle numbers, the amount of Al_2O_3 deposited is less than or equal to one monolayer. With such low Al_2O_3 loadings, the Al:Si surface ratio is limited by the amount of Al_2O_3 deposited, which in turn determines the number of Pd/Al interface sites. Thus, as the surface chemical composition transitions from SiO_2 to Al_2O_3, the reaction rate rapidly increases, driven by the favorable Pd/Al interfacial interaction compared to that of Pd/Si. With higher cycle numbers, the evolution of the bulk crystallinity of the Al_2O_3 influences the electronic structure of the support surface,[57] and thus impacts the Pd-support interaction. With a sufficiently thick Al_2O_3 coating, the formation of γ-Al_2O_3 improves the methane combustion properties of Pd. Notably, at high Al_2O_3 loadings, there is enough Al_2O_3 to form several monolayers, but the Si/Al intermixing

results in some Si at the surface of the support, leading to a lower reaction rate than for Pd on a bulk γ-Al$_2$O$_3$ support.
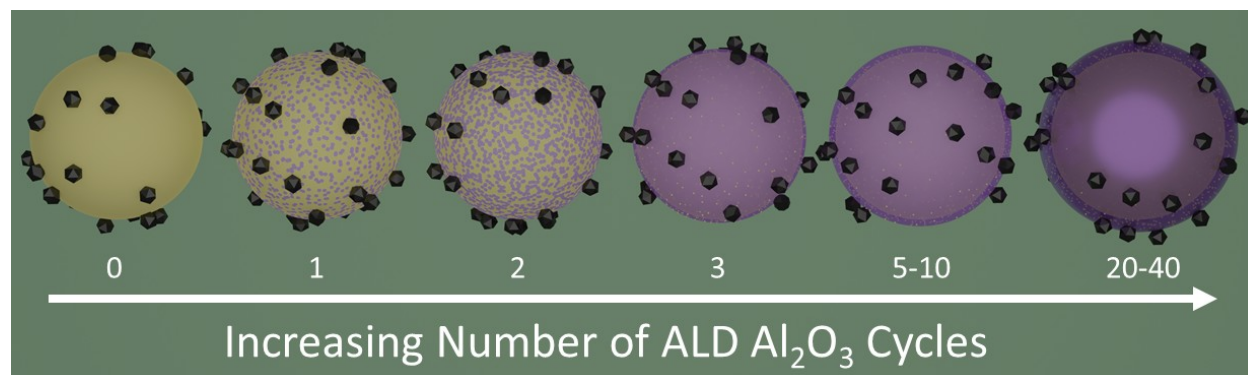

Figure 9. Schematic explanation of support transformation as a function of number of Al$_2$O$_3$ ALD cycles. (1) One monolayer of Al$_2$O$_3$ forms during the first 3 ALD cycles; (2) for thick Al$_2$O$_3$ layers, the support crystallizes to a γ-Al$_2$O$_3$ phase; (3) Si partially mixes into the Al$_2$O$_3$ coating.

Conclusion

In this work, we have developed a combined ALD and colloidal synthesis method to reveal the metal-support interactions that determine the methane combustion reactivity of SiO$_2$ and Al$_2$O$_3$ supported Pd. The Pd-support interface, specifically the relative amounts of Pd/Al and Pd/Si interface sites, significantly contribute to the overall reaction rate. The role of the interface chemistry is so dramatic that even sub-monolayer coverages of Al$_2$O$_3$ can significantly improve the methane combustion reactivity of Pd. The surface characteristics of the support are also influenced by the bulk properties of the underlying material. The crystal structure of Al$_2$O$_3$ also impacts the reaction rate, as seen in the comparison of amorphous and gamma alumina supports. Similarly, the bulk composition of the support, in this case defined by the Si/Al intermixing, can alter the electronic properties and chemical composition of the support surface, and thus impact Pd reactivity. The nature of the metal-support interactions and the classification of bulk and surface effects described in this work likely extend to other supported metal catalytic systems. The ALD-colloidal synthesis method employed here provides a general framework for model catalyst synthesis that can be applied to fundamental studies of metal-support interactions in many other catalyst systems.

Acknowledgements

Supporting Information

Supporting information includes additional reactivity measurements, microscopic characterization, details of IR analysis, and ALD growth curve of Al_2O_3.

Corresponding Author

Matteo Cargnello: mcargn@stanford.edu
Stacey Bent: sbent@stanford.edu

Notes

The authors declare no competing financial interest.

References

(1)   Foster, S. L.; Bakovic, S. I. P.; Duda, R. D.; Maheshwari, S.; Milton, R. D.; Minteer, S. D.; Janik, M. J.; Renner, J. N.; Greenlee, L. F. Catalysts for Nitrogen Reduction to Ammonia. *Nat. Catal.* **2018**, *1* (7), 490–500. https://doi.org/10.1038/s41929-018-0092-7.

(2)   Behrens, M.; Studt, F.; Kasatkin, I.; Kühl, S.; Hävecker, M.; Abild-pedersen, F.; Zander, S.; Girgsdies, F.; Kurr, P.; Kniep, B.; Tovar, M.; Fischer, R. W.; Nørskov, J. K.; Schlögl,

R. The Active Site of Methanol Synthesis over Cu/ZnO/Al2O3 Industrial Catalysts. *Science (80-.).* **2012**, *759* (May), 893–898.

(3)   van Deelen, T. W.; Hernández Mejía, C.; de Jong, K. P. Control of Metal-Support Interactions in Heterogeneous Catalysts to Enhance Activity and Selectivity. *Nat. Catal.* **2019**, *2* (11), 955–970. https://doi.org/10.1038/s41929-019-0364-x.

(4)   Ahmadi, M.; Mistry, H.; Roldan Cuenya, B. Tailoring the Catalytic Properties of Metal Nanoparticles via Support Interactions. *J. Phys. Chem. Lett.* **2016**, *7* (17), 3519–3533. https://doi.org/10.1021/acs.jpclett.6b01198.

(5)   Willis, J. J.; Gallo, A.; Sokaras, D.; Aljama, H.; Nowak, S. H.; Goodman, E. D.; Wu, L.; Tassone, C. J.; Jaramillo, T. F.; Abild-Pedersen, F.; Cargnello, M. Systematic Structure-Property Relationship Studies in Palladium-Catalyzed Methane Complete Combustion. *ACS Catal.* **2017**, *7* (11), 7810–7821. https://doi.org/10.1021/acscatal.7b02414.

(6)   Sereda, G.; Marshall, C.; Libera, J. A.; Dreessen, J.; Grady, A.; Turner, M. Effect of Atomic Layer Deposition Support Thickness on Structural Properties and Oxidative Dehydrogenation of Propane on Alumina- and Titania-Supported Vanadia. *Catal. Letters* **2012**, *142* (4), 399–407. https://doi.org/10.1007/s10562-012-0780-x.

(7)   Zhang, S.; Plessow, P. N.; Willis, J. J.; Dai, S.; Xu, M.; Graham, G. W.; Cargnello, M.; Abild-Pedersen, F.; Pan, X. Dynamical Observation and Detailed Description of Catalysts under Strong Metal-Support Interaction. *Nano Lett.* **2016**, *16* (7), 4528–4534. https://doi.org/10.1021/acs.nanolett.6b01769.

(8)   Cargnello, M.; Doan-nguyen, V. V. T.; Gordon, T. R.; Diaz, R. E.; Stach, E. A.; Gorte, R. J.; Fornasiero, P.; Murray, C. B.; Diaz, E.; Stach, A.; Gordon, T. R.; Rosa, E.; Stach, A. Control of Metal Nanocrystal Size Control of Metal Nanocrystal Size Reveals Interface Interface Reveals Role for Ceria Catalysts Role for Ceria Catalysts. **2013**, *341* (6147), 7–10.

(9)   Matsubu, J. C.; Zhang, S.; DeRita, L.; Marinkovic, N. S.; Chen, J. G.; Graham, G. W.; Pan, X.; Christopher, P. Adsorbate-Mediated Strong Metal-Support Interactions in Oxide-Supported Rh Catalysts. *Nat. Chem.* **2017**, *9* (2), 120–127. https://doi.org/10.1038/NCHEM.2607.

(10)   Yang, A. C.; Choksi, T.; Streibel, V.; Aljama, H.; Wrasman, C. J.; Roling, L. T.;

Goodman, E. D.; Thomas, D.; Bare, S. R.; Sánchez-Carrera, R. S.; Schäfer, A.; Li, Y.; Abild-Pedersen, F.; Cargnello, M. Revealing the Structure of a Catalytic Combustion Active-Site Ensemble Combining Uniform Nanocrystal Catalysts and Theory Insights. *Proc. Natl. Acad. Sci. U. S. A.* **2020**, *117* (26), 14721–14729. https://doi.org/10.1073/pnas.2002342117.

(11) Haller, G. L.; Resasco, D. E. Metal–Support Interaction: Group VIII Metals and Reducible Oxides. *Adv. Catal.* **1989**, *36* (C), 173–235. https://doi.org/10.1016/S0360-0564(08)60018-8.

(12) Porkovich, A.; Ziadi, Z.; Kumar, P.; Kioseoglou, J.; Jian, N.; Weng, L.; Steinhauer, S.; Vernieres, J.; Grammatikopoulos, P.; Sowwan, M. In Situ Observation of Metal to Metal Oxide Progression: A Study of Charge Transfer Phenomenon at Ru-CuO Interfaces. *ACS Nano* **2019**, *13* (11), 12425–12437. https://doi.org/10.1021/acsnano.9b06224.

(13) Yan, Q. Q.; Wu, D. X.; Chu, S. Q.; Chen, Z. Q.; Lin, Y.; Chen, M. X.; Zhang, J.; Wu, X. J.; Liang, H. W. Reversing the Charge Transfer between Platinum and Sulfur-Doped Carbon Support for Electrocatalytic Hydrogen Evolution. *Nat. Commun.* **2019**, *10* (1). https://doi.org/10.1038/s41467-019-12851-w.

(14) Losch, P.; Huang, W.; Goodman, E. D.; Wrasman, C. J.; Holm, A.; Riscoe, A. R.; Schwalbe, J. A.; Cargnello, M. Colloidal Nanocrystals for Heterogeneous Catalysis. *Nano Today* **2019**, *24*, 15–47.

(15) Huang, J.; Buonsanti, R. Colloidal Nanocrystals as Heterogeneous Catalysts for Electrochemical CO 2 Conversion †. *Chem. Mater.* **2019**, *31* (1), 13–25. https://doi.org/10.1021/acs.chemmater.8b04155.

(16) Pang, F.; Liu, X.; He, M.; Ge, J. Ag3PO4 Colloidal Nanocrystal Clusters with Controllable Shape and Superior Photocatalytic Activity. *Nano Res.* **2015**, *8* (1), 106–116. https://doi.org/10.1007/s12274-014-0580-2.

(17) Oneill, B. J.; Jackson, D. H. K.; Lee, J.; Canlas, C.; Stair, P. C.; Marshall, C. L.; Elam, J. W.; Kuech, T. F.; Dumesic, J. A.; Huber, G. W. Catalyst Design with Atomic Layer Deposition. *ACS Catal.* **2015**, *5* (3), 1804–1825. https://doi.org/10.1021/cs501862h.

(18) Singh, J. A.; Yang, N.; Bent, S. F. Nanoengineering Heterogeneous Catalysts by Atomic Layer Deposition. *Annu. Rev. Chem. Biomol. Eng.* **2017**, *8*, 41–62.

https://doi.org/10.1146/annurev-chembioeng-060816-101547.

(19)   Asundi, A. S.; Raiford, J. A.; Bent, S. F. Opportunities for Atomic Layer Deposition in Emerging Energy Technologies. *ACS Energy Lett.* **2019**, *4* (4), 908–925. https://doi.org/10.1021/acsenergylett.9b00249.

(20)   Zhang, B.; Qin, Y. Interface Tailoring of Heterogeneous Catalysts by Atomic Layer Deposition. *ACS Catal.* **2018**, *8*, 10064–10081. https://doi.org/10.1021/acscatal.8b02659.

(21)   Weng, Z.; Zaera, F. Atomic Layer Deposition (ALD) as a Way to Prepare New Mixed-Oxide Catalyst Supports: The Case of Alumina Addition to Silica-Supported Platinum for the Selective Hydrogenation of Cinnamaldehyde. *Top. Catal.* **2019**, *62* (12–16), 838–848. https://doi.org/10.1007/s11244-019-01163-4.

(22)   Yang, N.; Bent, S. F. Investigation of Inherent Differences between Oxide Supports in Heterogeneous Catalysis in the Absence of Structural Variations. *J. Catal.* **2017**, *351*, 49–58. https://doi.org/10.1016/j.jcat.2017.04.003.

(23)   Nathan, S. S.; Asundi, A. S.; Singh, J. A.; Hoffman, A. S.; Boubnov, A.; Hong, J.; Bare, S. R.; Bent, S. F. Understanding Support Effects of ZnO-Promoted Co Catalysts for Syngas Conversion to Alcohols Using Atomic Layer Deposition. *ChemCatChem* **2021**, *13* (2), 770–781. https://doi.org/10.1002/cctc.202001630.

(24)   Lampert, J. K.; Kazi, M. S.; Farrauto, R. J. Palladium Catalyst Performance for Methane Emissions Abatement from Lean Bum Natural Gas Vehicles. *Appl. Catal. B Environ.* **1997**, *14* (3–4), 211–223. https://doi.org/10.1016/S0926-3373(97)00024-6.

(25)   Farrauto, R. J. Low-Temperature Oxidation of Methane. *Science (80-.).* **2012**, *337* (August), 659–660.

(26)   Cargnello, M.; Delgado Jaén, J. J.; Hernández Garrido, J. C.; Bakhmutsky, K.; Montini, T.; Calvino Gámez, J. J.; Gorte, R. J.; Fornasiero, P. Exceptional Activity for Methane Combustion over Modular Pd@CeO2 Subunits on Functionalized Al2O3. *Science (80-.).* **2012**, *337* (6095), 713–717. https://doi.org/10.1126/science.1222887.

(27)   Murata, K.; Kosuge, D.; Ohyama, J.; Mahara, Y.; Yamamoto, Y.; Arai, S.; Satsuma, A. Exploiting Metal-Support Interactions to Tune the Redox Properties of Supported Pd Catalysts for Methane Combustion. *ACS Catal.* **2020**, *10* (2), 1381–1387. https://doi.org/10.1021/acscatal.9b04524.

(28)   Murata, K.; Mahara, Y.; Ohyama, J.; Yamamoto, Y.; Arai, S.; Satsuma, A. The Metal–
         Support Interaction Concerning the Particle Size Effect of Pd/Al2O3 on Methane
         Combustion. *Angew. Chemie - Int. Ed.* **2017**, *56* (50), 15993–15997.
         https://doi.org/10.1002/anie.201709124.

(29)   Schwartz, W. R.; Ciuparu, D.; Pfefferle, L. D. Combustion of Methane over Palladium-
         Based Catalysts: Catalytic Deactivation and Role of the Support. *J. Phys. Chem. C* **2012**,
         116 (15), 8587–8593. https://doi.org/10.1021/jp212236e.

(30)   Goodman, E. D.; Johnston-Peck, A. C.; Dietze, E. M.; Wrasman, C. J.; Hoffman, A. S.;
         Abild-Pedersen, F.; Bare, S. R.; Plessow, P. N.; Cargnello, M. Catalyst Deactivation via
         Decomposition into Single Atoms and the Role of Metal Loading. *Nat. Catal.* **2019**, *2* (9),
         748–755. https://doi.org/10.1038/s41929-019-0328-1.

(31)   Stober, W.; Fink, A. Controlled Growth of Monodispere Silica Spheres in the Micron Size
         Range. *J. Colloid Interface Sci.* **1968**, *26*, 62–69.

(32)   Goodman, E. D.; Carlson, E. Z.; Dietze, E. M.; Tahsini, N.; Johnson, A.; Aitbekova, A.;
         Nguyen Taylor, T.; Plessow, P. N.; Cargnello, M. Size-Controlled Nanocrystals Reveal
         Spatial Dependence and Severity of Nanoparticle Coalescence and Ostwald Ripening in
         Sintering   Phenomena.   *Nanoscale*   **2021**,   *13*   (2),   930–938.
         https://doi.org/10.1039/d0nr07960j.

(33)   Libera, J. A.; Elam, J. W.; Pellin, M. J. Conformal ZnO Coatings on High Surface Area
         Silica Gel Using Atomic Layer Deposition. *Thin Solid Films* **2008**, *516* (18), 6158–6166.

(34)   Onn, T. M.; Küngas, R.; Fornasiero, P.; Huang, K.; Gorte, R. J. Atomic Layer Deposition
         on Porous Materials: Problems with Conventional Approaches to Catalyst and Fuel Cell
         Electrode Preparation. *Inorganics* **2018**, *6* (1). https://doi.org/10.3390/inorganics6010034.

(35)   Detavernier, C.; Dendooven, J.; Pulinthanathu Sree, S.; Ludwig, K. F.; Martens, J. A.
         Tailoring Nanoporous Materials by Atomic Layer Deposition. *Chem. Soc. Rev.* **2011**, *40*
         (11), 5242–5253. https://doi.org/10.1039/c1cs15091j.

(36)   Soled, S. Silica-Supported Catalysts Get a New Breath of Life. *Science (80-.).* **2015**, *350*
         (6265), 1171–1172. https://doi.org/10.1126/science.aad2204.

(37)   Gaita, R.; Al-Bazi, S. J. An Ion-Exchange Method for Selective Separation of Palladium,
         Platinum and Rhodium from Solutions Obtained by Leaching Automotive Catalytic

Converters. *Talanta* **1995**, *42* (2), 249–255.

(38)   Herreros, J. M.; Gill, S. S.; Lefort, I.; Tsolakis, A.; Millington, P.; Moss, E. . Enhancing the Low Temperature Oxidation Performance over a Pt and Pt-Pd Diesel Oxidation Catalyst. *Appl. Catal. B Environ.* **2014**, *147*, 835–841.

(39)   Puurunen, R. L. Surface Chemistry of Atomic Layer Deposition: A Case Study for the Trimethylaluminum/Water Process. *J. Appl. Phys.* **2005**, *97* (12). https://doi.org/10.1063/1.1940727.

(40)   Van Helden, A. K.; Jansen, J. W.; Vrij, A. Preparation and Characterization of Spherical Monodisperse Silica Dispersions in Nonaqueous Solvents. *J. Colloid Interface Sci.* **1981**, *81* (2), 354–368. https://doi.org/10.1016/0021-9797(81)90417-3.

(41)   O'Connell, K.; Regalbuto, J. R. High Sensitivity Silicon Slit Detectors for 1 Nm Powder XRD Size Detection Limit. *Catal. Letters* **2015**, *145* (3), 777–783. https://doi.org/10.1007/s10562-015-1479-6.

(42)   Li, J.; Sun, J. Application of X-Ray Diffraction and Electron Crystallography for Solving Complex Structure Problems. *Acc. Chem. Res.* **2017**, *50* (11), 2737–2745. https://doi.org/10.1021/acs.accounts.7b00366.

(43)   Jakschik, S.; Schroeder, U.; Hecht, T.; Gutsche, M.; Seidl, H.; Bartha, J. W. Crystallization Behavior of Thin ALD-Al2O3 Films. *Thin Solid Films* **2003**, *425* (1–2), 216–220. https://doi.org/10.1016/S0040-6090(02)01262-2.

(44)   Cappella, A.; Battaglia, J. L.; Schick, V.; Kusiak, A.; Lamperti, A.; Wiemer, C.; Hay, B. High Temperature Thermal Conductivity of Amorphous Al2O 3 Thin Films Grown by Low Temperature ALD. *Adv. Eng. Mater.* **2013**, *15* (11), 1046–1050. https://doi.org/10.1002/adem.201300132.

(45)   Murata, K.; Ohyama, J.; Yamamoto, Y.; Arai, S.; Satsuma, A. Methane Combustion over Pd/Al2O3Catalysts in the Presence of Water: Effects of Pd Particle Size and Alumina Crystalline Phase. *ACS Catal.* **2020**, *10* (15), 8149–8156. https://doi.org/10.1021/acscatal.0c02050.

(46)   Lee, S. K.; Park, S. Y.; Yi, Y. S.; Moon, J. Structure and Disorder in Amorphous Alumina Thin Films: Insights from High-Resolution Solid-State NMR. *J. Phys. Chem. C* **2010**, *114* (32), 13890–13894. https://doi.org/10.1021/jp105306r.

(47)   Ren, J.; Zhang, L.; Eckert, H. Medium-Range Order in Sol − Gel Prepared Al2O3 − SiO2 Glasses: New Results from Solid-State NMR. *J. Phys. Chem. C* **2014**, *118*, 4906–4917.

(48)   Tao, Q.; Overhage, K.; Jursich, G.; Takoudis, C. On the Initial Growth of Atomic Layer Deposited TiO 2 Films on Silicon and Copper Surfaces. *Thin Solid Films* **2012**, *520* (22), 6752–6756. https://doi.org/10.1016/j.tsf.2012.07.004.

(49)   Puurunen, R. L.; Vandervorst, W. Island Growth as a Growth Mode in Atomic Layer Deposition: A Phenomenological Model. *J. Appl. Phys.* **2004**, *96* (12), 7686–7695. https://doi.org/10.1063/1.1810193.

(50)   Puurunen, R. L.; Vandervorst, W.; Besling, W. F. A.; Richard, O.; Bender, H.; Conard, T.; Zhao, C.; Delabie, A.; Caymax, M.; De Gendt, S.; Heyns, M.; Viitanen, M. M.; De Ridder, M.; Brongersma, H. H.; Tamminga, Y.; Dao, T.; De Win, T.; Verheijen, M.; Kaiser, M.; Tuominen, M. Island Growth in the Atomic Layer Deposition of Zirconium Oxide and Aluminum Oxide on Hydrogen-Terminated Silicon: Growth Mode Modeling and Transmission Electron Microscopy. *J. Appl. Phys.* **2004**, *96* (9), 4878–4889. https://doi.org/10.1063/1.1787624.

(51)   Nemana, S.; Gates, B. C. Surface-Mediated Synthesis and Spectroscopic Characterization of Tantalum Clusters on Silica. *Langmuir* **2006**, *22* (19), 8214–8220. https://doi.org/10.1021/la0609322.

(52)   Morrow, B. A.; Cody, I. A. Infrared Spectra of the Isolated Hydroxyl Groups on Silica. *J. Phys. Chem.* **1973**, *77* (11), 1465–1467. https://doi.org/10.1021/j100630a027.

(53)   Efimov, A. M.; Pogareva, V. G. IR Absorption Spectra of Vitreous Silica and Silicate Glasses: The Nature of Bands in the 1300 to 5000 Cm- 1 Region. *Chem. Geol.* **2006**, *229* (1–3), 198–217. https://doi.org/10.1016/j.chemgeo.2006.01.022.

(54)   Zhang, M.; Salje, E. K. H.; Ewing, R. C. Infrared Spectra of Si-O Overtones, Hydrous Species, and U Ions in Metamict Zircon: Radiation Damage and Recrystallization. *J. Phys. Condens. Matter* **2002**, *14* (12), 3333–3352. https://doi.org/10.1088/0953-8984/14/12/319.

(55)   Mawhinney, D. B.; Glass, J. A.; Yates, J. T. FTIR Study of the Oxidation of Porous Silicon. *J. Phys. Chem. B* **1997**, *101* (7), 1202–1206. https://doi.org/10.1021/jp963322r.

(56)   Iatsunskyi, I.; Kempiński, M.; Jancelewicz, M.; Załęski, K.; Jurga, S.; Smyntyna, V. Structural and XPS Characterization of ALD Al2O3 Coated Porous Silicon. *Vacuum*

2015, *113*, 52–58. https://doi.org/10.1016/j.vacuum.2014.12.015.

(57)   Perevalov, T. V.; Gritsenko, V. A.; Kaichev, V. V. Electronic Structure of Aluminum Oxide: Ab Initio Simulations of α and γ Phases and Comparison with Experiment for Amorphous Films. *EPJ Appl. Phys.* **2010**, *52* (3). https://doi.org/10.1051/epjap/2010159.